Robotica (2024), 1–19
doi:10.1017/S0263574724001644

CAMBRIDGE UNIVERSITY PRESS

RESEARCH ARTICLE

Vision-based dynamic modeling of wheeled-legged robot considering slippage using Gibbs–Appell formulation

M. H. Korayem, N. Nikseresht and A. H. Asadi

Robotics Research Laboratory, Center of Excellence in Experimental Solid Mechanics and Dynamics, School of Mechanical Engineering, Iran University of Science and Technology, Tehran, Iran
Corresponding author: M. H. Korayem; Email: hkorayem@iust.ac.ir

Received: 28 April 2024; **Revised:** 11 July 2024; **Accepted:** 19 August 2024

Keywords: Wheeled-legged robot; Gibbs–Appell; pose estimation; wheel slippage; dynamic modeling; machine vision; quasi coordinate

Abstract

This study focuses on the kinematic and dynamic modeling of a wheeled-legged robot (WLR), taking into account kinematic and dynamic slippage. In this regard, the Gibbs–Appell formulation was utilized to derive dynamic equations. Determining the slippage in the wheels for movement equations is a challenging task due to its dependency on factors such as the robot's postures, velocities, and surface characteristics. To address this challenge, machine vision was used to quantify the slippage of the wheels on the body based on the pose estimation method. This data served as input for movement equations to analyze the robot's deviation from its path and posture. In the following, the robot's movement was simulated using Webots and MATLAB, followed by various experimental tests involving acceleration and changes in leg angles on the WLR. The results were then compared to the simulations to demonstrate the accuracy of the developed system modeling. Additionally, an IMU sensor was utilized to measure the robot's motion and validate against machine vision data. The findings revealed that neglecting the slippage of the wheels in the robot's motion modeling resulted in errors ranging from 5% to 11.5%. Furthermore, lateral slippage ranging from 1.1 to 5.2 cm was observed in the robot's accelerated movement. This highlights the importance of including lateral slippage in the equations for a more precise modeling of the robot's behavior.

1. Introduction

Wheeled-legged robots (WLR) are a type of mobile robot equipped with wheels attached to legs, enabling them to maintain balance while navigating paths with varying surface conditions. These versatile robots exhibit the ability to traverse slippery paths, surmount obstacles, ascend steep inclines, and maneuver through challenging terrains such as rocky landscapes, sand, and gravel. Achieving such capabilities requires a comprehensive understanding of the system's model and the dynamic environmental factors at play. Recent research endeavors have been dedicated to enhancing the functionality of these robots by developing new mechanisms, refining their models for improved accuracy, considering potential disturbances through the integration of diverse sensors and algorithms, and designing effective control strategies. This foundational research is essential for progressing toward the ultimate objective of creating fully autonomous WLRs.

As it is mentioned, many of recent research efforts have focused on the development of novel mechanisms as it directly influences the robot's performance, adaptability, and ability to overcome obstacles. In this regard, Thomas et al. have studied a wheeled mechanism that optimally distributes forces between wheels to improve vehicle performance and assist in automated robot missions. They created mathematical models for wheel movements and obstacle traversal, determining necessary motor torque [1]. The mechanism employed in this study aligns with the research conducted in this field, and the system equations have been extended for sliding motions [2]. Some researchers have enhanced wheeled robot

capabilities by increasing the number of degrees of freedom. Niu et al. introduced a six-degree-of-freedom wheeled robot with three degrees of freedom per leg, improving movement with prismatic joints. The robot demonstrated potential for mission execution through simulation and testing [3]. Additionally, Reid et al. in [4] have developed a wheeled robot with thirty-two degrees of freedom, tested on various terrains. The robot utilized wheel rolling, walking, and rotation modes to actively control load, orientation, and workspace. Real-time analysis using body sensors provided insights into the suspension system's performance. Furthermore, researchers have emphasized hybrid mechanisms by installing various types of wheels and other types of actuators to enhance robot functionality, enabling capabilities such as leaping and jumping while in motion [5, 6].

In the next step, researchers have worked on modeling the system to build the fundamentals of control system development, performance optimization, and enhancing terrain adaptability. In this context, in one of the similar research studies, Toorani et al. have focused on the dynamic modeling of a reconfigurable WLR using a geometric constraint based on the independent Gibbs–Appell formulation. They have proposed a method for analyzing the kinematics and dynamics of this type of robot, emphasizing the application of the Gibbs–Appell formulation to derive motion equations for the nonholonomic wheeled mobile robotic manipulator with revolute–prismatic joints [7]. As another application of the Gibbs–Appell formulation, Mirzaeinejad et al. have used the recursive Gibbs–Appell method to derive the kinematic and dynamic models of a wheeled mobile robot (WMR). The Gibbs–Appell method is then used to obtain the equations of motion for the WMR, which serve as the basis for developing new kinematics- and dynamics-based multivariable controllers [8]. Additionally, Mata et al. have utilized the Gibbs–Appell formulation to derive the equations of motion for the robot, which are subsequently used to develop two efficient algorithms for computing the required joint torques to achieve a desired motion. By employing the Gibbs–Appell method, the proposed algorithms can determine the inverse dynamics without the need for symbolic computation or numerical integration, thus making them computationally efficient and suitable for real-time control applications [9]. Korayem et al. have focused on the stability analysis of a WLR. The authors have proposed a novel force-angle method for stability analysis, which considers the position of the center of mass relative to the geometric center of the robot as an independent degree of freedom [10]. Aaron et al. have developed a hybrid wheeled robot for rough terrains, incorporating a leg-wheel system based on Denavit–Hartenberg parameters. They have created a kinematic model, analyzed degrees of freedom, and studied wheel-leg movement. Also, validated their findings with simulation results in Adams software [11]. Alamdari et al. have enhanced the motion capabilities of the wheeled walking robot, HiLoS, by analyzing kinematics, dynamics, and path planning equations. They found wheel slip to be a crucial stability factor and determined stability criteria based on platform orientation and joint configurations. By applying kinematic and dynamic equations, they achieved path planning and motion control for the robot [12]. Doe et al. have developed a new method for wheel movements in a walking robot to improve body tracking. By controlling torque, the robot can navigate uneven surfaces. They used spatial vectors to extract contact and kinematic models and combined them for precise wheel movements tailored to different conditions. Multiple algorithms were created to analyze the robot's structure effectively [13]. Additionally, Reid et al. in [14] have adjusted the wheeled robot's suspension system using inverse kinematics and terrain mapping for adaptability. They also analyzed images from a camera and light sensor, focusing on deliberate movement aligned with real-world behavior.

Moreover, a significant portion of recent research has been dedicated to improving control strategies to achieve the final goal of enhancing robot maneuverability and movement. To exploit the capabilities of hybrid mechanisms in robots, Reid et al. in [4] have developed an algorithm for a hybrid wheeled robot to navigate uneven paths by shifting weight between legs to maintain stability. This involved lifting one leg at a time while the other three legs bear the weight, using load redistribution to align the center of gravity with the center of pressure for balance and smooth motion. Moreover, in determining appropriate degrees of freedom and mechanical relationships, Grand et al. have optimized the locomotion of the HiLoS planetary exploration robot, an early wheeled walking robot. Subsequently, they developed a control method for improving traction torque, leading to increased robot stability. Their approach

https://doi.org/10.1017/S0263574724001644 Published online by Cambridge University Press

was validated through practical experiments and dynamic simulations, demonstrating the robot's performance on solid and soft terrain like sand [15]. Beckman et al. have investigated the MHT wheeled walking robot, which features an adjustable body center of gravity. Designed for improved mobility on uneven terrain, this robot's two-dimensional dynamic stability was studied. It can dynamically shift its center of gravity parallel to the forward direction, move smoothly on flat ground, and employs hydraulic actuators for leg joints [16]. Additionally, some researchers have focused on enhancing the movement capabilities of robots on challenging terrains through advanced path planning and optimization techniques. Medeiros et al. [17] have developed a sophisticated animal robot by combining wheel speed with leg capabilities and optimizing actuator forces based on terrain information, while Ishigami et al. [18] have created a path planning algorithm for wheeled robots considering wheel slip dynamics and soil properties. In another similar research, Bjelonic et al. have presented an online path optimization framework for wheeled ground robots capable of executing fast movement strategies. Their robot quickly maps the environment and selects the best possible path for robot movement among other available paths [19]. Considering the fact that slippage can play a significant role in the locomotion of robots, several researchers have considered this issue in the controlling process [20–23]. Also, in order to estimate and predict the slip, several research have been conducted [24–27]. They have utilized various techniques such as artificial neural networks, image processing, Doppler radar, and computer vision to predict, compensate for, and estimate wheel slip, friction, traction forces, and wheel-to-ground contact angles. Additionally, Reina et al. in [28–29] have used methods like deep learning, six-dimensional positional estimation, and machine vision-based algorithms to measure displacement, position, lateral slip, and sinkage of the robots, ultimately aiming to enhance the accuracy and efficiency of mobile robots moving on challenging terrains. This paper presents the development of a system model for a WLR, highlighting three key innovations.

1. The Gibbs–Appell method is used to simplify rotational angle constraints for the robot's body, avoiding complex equations and reducing the computational burden. Assumptions are made to develop constraint equations and calculate Gibbs functions, allowing for dynamic and slippage equations for each wheel to be obtained without determining Lagrangian coefficients. Also, this method requires fewer partial derivatives to calculate joint torque by quasi-coordinates. To the best of our knowledge, this is the first application of the Gibbs–Appell formulation on the presented system with consideration of slippage in moving robots.
2. A machine vision method known as pose estimation to accurately estimate the slippage occurring on the robot's wheels is used. This method proved to be more effective in reducing the amount of error compared to classical methods.
3. Performance of the developed model has been evaluated under different circumstances using MATLAB and Webots and compared with the results of experimental tests.

The paper is organized as follows: Section two provides an overview of the mechatronic components of the robot, as well as a description of the methodology utilized to estimate actual slippage during experimental tests. Section three presents the development of kinematic equations for the robot, incorporating kinematic slippage as a slip ratio. Additionally, dynamic equations are derived taking into account slippage, using the Coulomb friction model. In Section four, the results of simulations based on the developed equations are presented and compared with the robot's behavior during experimental tests to assess performance and validate the accuracy of the theoretical framework.

2. Description of the robot and detection method

2.1. Robot structure

As it illustrated in Fig. 1, the WLR analyzed in this study features 8 degrees of freedom, with 2 degrees of freedom allocated to each joint (wheel-leg). Constructed from aluminum sheets and plexiglass,

https://doi.org/10.1017/S0263574724001644 Published online by Cambridge University Press

Table I. *Actual parameters of WLR.*

Parameters	Symbol	Value	Unit
Length of WLR	l_x	0.35	m
Width of WLR	l_y	0.32	m
Length of leg	l	0.135	m
Radius of wheel	a	0.034	m
Mass of WLR's body	M_G	2.8	kg
Moment of inertia of wheel about its axis	I_o	0.00028	kgm^2
Moment of inertia of WLR's body about Y-axis	I_{Gy}	0.00002	kgm^2
Moment of inertia of WLR's body about Z-axis	I_{Gz}	0.00003	kgm^2
Moment of inertia of WLR's leg about X-axis	I_{lx}	0.00012	kgm^2
Moment of inertia of WLR's leg about Y-axis	I_{ly}	0.00012	kgm^2

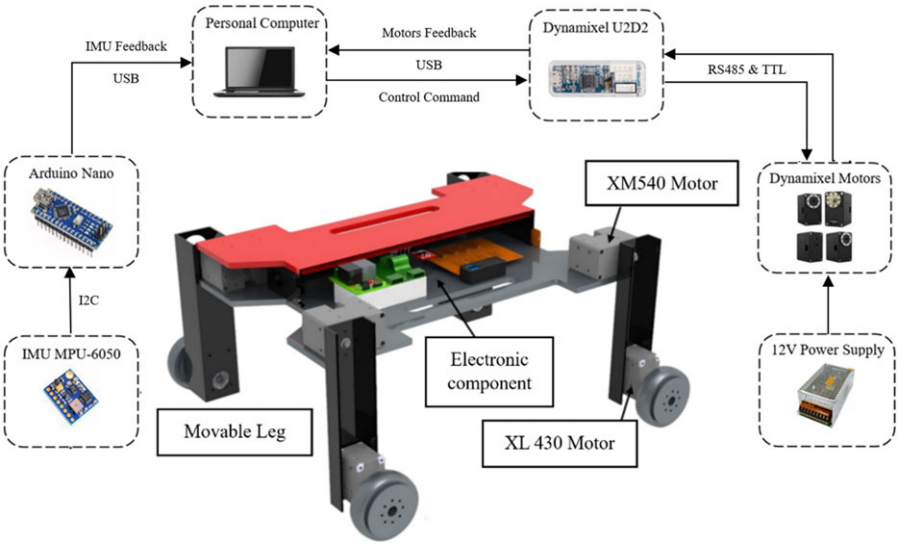

Figure 1. *Schematic of the robot components and its electronic circuit.*

the robot's body incorporates an aluminum sheet in the lower section, which serves to lower the center of gravity and house electronic components, while plexiglass sheets are utilized as body covers. The body dimensions measure 7 × 35 × 32 cms, with the legs measuring 13.5 × 5 × 5 cms. The robot's weight, excluding the power source, amounts to 3 kgs. The wheels, with a diameter of 6.8 cms, are specifically designed with a tread pattern to enhance rotation on sloping and slippery surfaces, thereby augmenting the wheels' friction with the terrain. Mechatronic components include 8 Dynamixel motors, each with a power rating of 150 W; this comprises four XM540-W150-R motors for hip joints and four XL430-W250-T motors for the wheels. These motors are capable of transmitting feedback on position, speed, and torque to the PC. The internal motor gearboxes directly link the wheels and legs, while the electronic elements are contained in the main body of the robot. An accelerometer and gyroscope, the MPU-6050, serve as a 6-axis IMU sensor to determine the posture and position of the robot's center of mass. The PC acts as the main controller for the robot, receiving all analog and digital inputs and outputs, allowing commands to be issued to the actuators of the wheels and legs. Table I shows the actual parameters of WLR.

https://doi.org/10.1017/S0263574724001644 Published online by Cambridge University Press

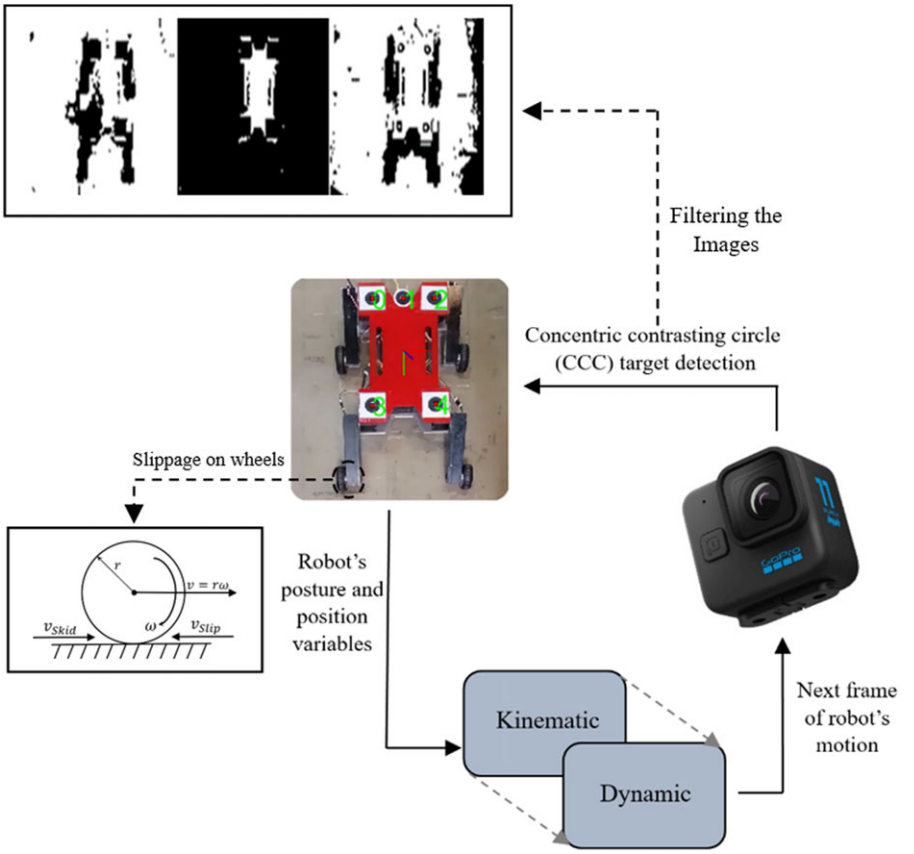

Figure 2. *Schematic of the slip estimation process.*

2.2. Vision method

The effect of slippage on wheeled robots during accelerated movements can result in significant errors between the expected and actual outcomes. Fig. 2 illustrates the application of pose estimation method along with concentric circles to assess the displacement of robot movement and body slippage in a controlled laboratory setting. To address the challenges posed by noise and varying lighting conditions, this method was employed to track the position of the robot body in captured images. By identifying and averaging the coordinates of the centers of the circles, a virtual coordinate system was established at the midpoint of the circles on the robot body, enabling the calculation of displacement for that specific point. By comparing the robot's movement trajectory with the intended path, we are able to quantify the extent of body slippage. Deviation from the path and failure to reach the final destination of the robot is caused by two factors, slipping and skidding. The direction vectors of these two factors are opposite to each other, and separating them from each other is difficult. Therefore, these two factors have been measured together as the slip of the robot's wheels and have been incorporated into the robot's equations.

3. System model development

This section focuses on the modeling and derivation of kinematic and dynamic equations for the WLR, assuming the presence of wheel slippage. Kinematic equations are extracted using the vector-based method, while dynamic equations are derived using the Gibbs–Appell method. By utilizing pseudo-acceleration equations and Gibbs functions, the forces and torques acting on the robot's actuators are

https://doi.org/10.1017/S0263574724001644 Published online by Cambridge University Press

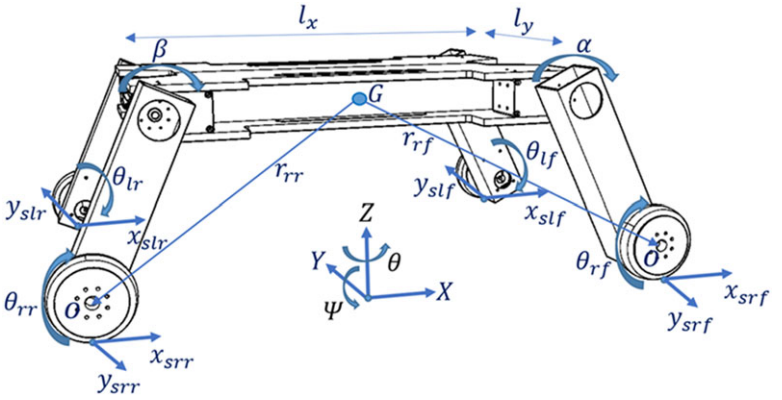

Figure 3. *Schematic of the WLR [28].*

determined. The effects of kinematic slippage are incorporated into the equations as a slip ratio, and the dynamic effects of slippage resulting from insufficient friction force are simplified by using the Coulomb friction model due to the complexity of the WLR equations.

Fig. 3 schematically shows the robot along with its parameters and coordinates, where $\boldsymbol{r_{lf}}$, $\boldsymbol{r_{rf}}$ are the vectors representing the centers of the left and right front wheels relative to the center of the platform, and $\boldsymbol{r_{lr}}$, $\boldsymbol{r_{rr}}$ are the vectors representing the centers of the left and right rear wheels relative to the center of the platform. θ_{lf}, θ_{rf}, θ_{lr}, θ_{rr} are the angles of rotation of the front left and right wheels and the rear left and right wheels, and α, β are the angles of rotation of the two front feet and the two rear feet, with their positive directions being counterclockwise. G is the center of mass of the robot, while l_x, l_y are the length and width of the robot body and O is the center of the wheels. Ψ is the angle of rotation around the Y-axis of the robot body and θ is the angle of rotation around the Z-axis of the robot body. x_{slf}, x_{srf}, x_{slr}, x_{srr} are the longitudinal slippage of the front left and right wheels and the rear left and right wheels also y_{slf}, y_{srf}, y_{slr}, y_{srr} are the lateral slippage of the front left and right wheels and the rear left and right wheels and Z_{slf}, Z_{srf}, Z_{slr}, Z_{srr} represent the slippage in the vertical direction of the front left and right wheels and the rear left and right wheels of the robot, respectively. Which these variables are extracted using machine vision to monitor the robot's movement. The robot's coordinate frame is considered on the moving surface along the center of mass of the robot, with the X-axis along the length, the Y-axis along the width and the Z-axis along the height changes. Additionally, a represents the radius of the wheels, and l denotes the length of the legs. In this article, the wheel-legged robot is modeled using simplifying assumptions to streamline the analysis. In comparison to other wheel-legged robots, this particular robot has a reduced number of degrees of freedom. The legs of the robot utilize single-link joints instead of more complex double-link knee joints, with the waist joint and wheel steering joints being omitted from the model. To further simplify the modeling process, the rotation angles of the front legs and rear legs are assumed to be uniform within each set. Consequently, rotation around the x-axis is disregarded, as the robot's body is not expected to rotate along this axis under these specific conditions. Moreover, the rear wheels of the robot are assumed to freely spin without external input to prevent oversteering.

3.1. Kinematics of the WLR

By writing the position vectors of the wheels relative to the center of mass of the robot and taking derivatives of them, we determine the relative speeds of the wheels relative to its center of mass and obtain the speeds of the wheels and legs of the robot (point O). In Eq. (1a), $\boldsymbol{v}$ is the speed of the center of the wheels and legs of the robot (point O) [30].

$$\boldsymbol{v} = \boldsymbol{v_G} + \dot{\theta}\hat{\boldsymbol{k}} \times \boldsymbol{r_{O/G}} + \boldsymbol{v_{O/G}} \tag{1}$$

https://doi.org/10.1017/S0263574724001644 Published online by Cambridge University Press

where $\boldsymbol{v_G}$ represents the center of mass velocity of the platform, $\boldsymbol{r_{O/G}}$ denotes the vector connecting the wheel center to the center of mass, and $\boldsymbol{v_{O/G}}$ signifies the relative velocity of the wheel with respect to the platform. We decompose the robot's body velocity along the coordinate axes as follows:

$$(\boldsymbol{v_G})_x = \dot{x},\ (\boldsymbol{v_G})_y = \dot{y},\ (\boldsymbol{v_G})_z = \dot{z} \tag{2}$$

By writing Eq. (1) for each of the wheels and incorporating the linear velocities of the wheels and their slip components on the opposite side, the kinematic equations for the robot, assuming longitudinal, lateral and vertical slips, take the form of Eq. (3–6):

Front right wheel velocity:

$$\boldsymbol{v_{rf}} = \left(\dot{x} - \dot{x}_{srf} - a\dot{\theta}_{rf}\right)\hat{\boldsymbol{i}} + \left(\dot{y} - \dot{y}_{srf}\right)\hat{\boldsymbol{j}} + \left(\dot{z} - \dot{z}_{srf}\right)\hat{\boldsymbol{k}} + \dot{\theta}\hat{\boldsymbol{k}} \times \boldsymbol{r_{rf}} + \dot{\boldsymbol{r}}_{\boldsymbol{rf}} \tag{3}$$

Front left wheel velocity:

$$\boldsymbol{v_{lf}} = \left(\dot{x} - \dot{x}_{slf} - a\dot{\theta}_{lf}\right)\hat{\boldsymbol{i}} + \left(\dot{y} - \dot{y}_{slf}\right)\hat{\boldsymbol{j}} + \left(\dot{z} - \dot{z}_{slf}\right)\hat{\boldsymbol{k}} + \dot{\theta}\hat{\boldsymbol{k}} \times \boldsymbol{r_{lf}} + \dot{\boldsymbol{r}}_{\boldsymbol{lf}} \tag{4}$$

Rear right wheel velocity:

$$\boldsymbol{v_{rr}} = \left(\dot{x} - \dot{x}_{srr} - a\dot{\theta}_{rr}\right)\hat{\boldsymbol{i}} + (\dot{y} - \dot{y}_{srr})\hat{\boldsymbol{j}} + (\dot{z} - \dot{z}_{srr})\hat{\boldsymbol{k}} + \dot{\theta}\hat{\boldsymbol{k}} \times \boldsymbol{r_{rr}} + \dot{\boldsymbol{r}}_{\boldsymbol{rr}} \tag{5}$$

Rear left wheel velocity:

$$\boldsymbol{v_{lr}} = \left(\dot{x} - \dot{x}_{slr} - a\dot{\theta}_{lr}\right)\hat{\boldsymbol{i}} + (\dot{y} - \dot{y}_{slr})\hat{\boldsymbol{j}} + (\dot{z} - \dot{z}_{slr})\hat{\boldsymbol{k}} + \dot{\theta}\hat{\boldsymbol{k}} \times \boldsymbol{r_{lr}} + \dot{\boldsymbol{r}}_{\boldsymbol{lr}} \tag{6}$$

In the following, we proceed by differentiating the above relations and determining the accelerations to formulate the dynamic equations.

3.2. Dynamics of the WLR

The Gibbs–Appell method has been used to obtain the dynamic equations. The pseudo-coordinates of the problem are determined and then the system accelerations are extracted in terms of pseudo-coordinates. Next, the Gibbs functions for different parts of the robot are determined and by putting them into the Gibbs equation and taking derivatives with respect to each of the pseudo accelerations, the dynamic equations of the robot are extracted. The pseudo-coordinates are α, β, θ_{rf}, θ_{lf}, θ_{rr}, θ_{lr}, x_{slf}, x_{srf}, x_{slr}, x_{srr}, y_l, y_r with derivatives from the Gibbs–Appell equations in terms of pseudo accelerations, which are second-order derivatives of the pseudo-coordinates, the governing dynamic equations of the system are obtained. The Gibbs functions are determined separately for the three main parts of the robot.

Gibbs function for wheels:

$$S_1 = \frac{I_o}{2}\left(\ddot{\theta}_{rf}^2 + \ddot{\theta}_{lf}^2 + \ddot{\theta}_{rr}^2 + \ddot{\theta}_{lr}^2\right) \tag{7}$$

Gibbs function for legs:

$$S_2 = I_{ly}\left(\ddot{\alpha}^2 + \ddot{\beta}^2\right) + I_{lx}\ddot{\theta}^2\left(cos^2\alpha + cos^2\beta\right) + \frac{m_l}{2}\left(a_{rf}^2 + a_{lf}^2 + a_{rr}^2 + a_{lr}^2\right) \tag{8}$$

Gibbs function for the body [7]:

$$S_3 = \frac{1}{2}\left(I_{Gz}\ddot{\theta}^2 + I_{Gy}\ddot{\Psi}^2 + M_G\boldsymbol{a_G}^2\right) \tag{9}$$

The final Gibbs function is obtained by combining Eq. (7–9):

$$\begin{aligned} S = {} & \frac{I_o}{2}\left(\ddot{\theta}_{rf}^2 + \ddot{\theta}_{lf}^2 + \ddot{\theta}_{rr}^2 + \ddot{\theta}_{lr}^2\right) + I_{ly}\left(\ddot{\alpha}^2 + \ddot{\beta}^2\right) + I_{lx}\ddot{\theta}^2\left(cos^2\alpha + cos^2\beta\right) + \frac{m_l}{2}\left(a_{rf}^2 + a_{lf}^2 + a_{rr}^2 + a_{lr}^2\right) \\ & + \frac{1}{2}\left(I_{Gz}\ddot{\theta}^2 + I_{Gy}\ddot{\Psi}^2 + M_G a_G^2\right) \end{aligned} \tag{10}$$

In the above equations, $I_o$is the wheel axis moment of inertia, I_{ly} is the leg Y-axis moment of inertia, I_{lx} is the leg X-axis moment of inertia, m_l is the leg mass, a_{lf}, a_{rf}, a_{lr}, a_{rr} are the accelerations of each

https://doi.org/10.1017/S0263574724001644 Published online by Cambridge University Press

leg, I_{Gz} is the body Z-axis moment of inertia, I_{Gy} is the body Y-axis moment of inertia, M_G is the robot body mass, and a_G is the acceleration of the robot's center of mass, which is calculated as a vector from the following equation:

$$a_G = \ddot{x}\hat{\boldsymbol{i}} + \ddot{y}\hat{\boldsymbol{j}} + \ddot{z}\hat{\boldsymbol{k}} + \dot{\theta}\hat{\boldsymbol{k}} \times \dot{x}\hat{\boldsymbol{i}} \tag{11}$$

In which, $\ddot{x}$, $\ddot{y}$, $\ddot{z}$ represent the accelerations of the robot's center of mass along the coordinate axes. Subsequently, the potential energy function of the system is calculated as follows:

$$V = gl(m_l\,(sin\,(\alpha) + sin\,(\beta)) + \frac{M_G}{2}(sin\,(\alpha + \Psi) + sin\,(\beta + \Psi)\,)) \tag{12}$$

where g represents the acceleration due to gravity. To determine dynamic slip or traction force, due to the complexity of relationships, a simplified model of the Dahl friction is employed under quasi-static conditions, which transforms into the Coulomb friction equation [31]:

$$F_{slip} = -\sigma_0 \hat{z} \tag{13}$$

Here, σ_0 denotes the surface roughness coefficient, and $\hat{z}$ represents relative displacement. In the static case, Eq. (13) becomes the following expression for Coulomb friction force [32]:

$$F_{slip} = -\mu_d F_n sgn\,(\upsilon) \tag{14}$$

where μ_d is the coefficient of dynamic friction, F_n is the normal force on the wheel surface, and υ is the linear velocity of the wheels. The friction function for the Gibbs–Appell equations is defined as:

$$\begin{aligned} D = {} & \mu_{dx}(F_{nf}\left(\dot{x}_{srf} sgn\left(\dot{x}_{srf}\right) + \dot{x}_{slf} sgn\left(\dot{x}_{slf}\right)\right) + F_{nr}\,(\dot{x}_{srr} sgn\,(\dot{x}_{srr}) + \dot{x}_{slr} sgn\,(\dot{x}_{slr})) \\ & + 2\mu_{dy}(F_{nf}\dot{y}_f sgn\left(\dot{y}_f\right) + F_{nr}\dot{y}_r sgn\,(\dot{y}_r)\,) \end{aligned} \tag{15}$$

In this equation, μ_{dx} represents the longitudinal friction coefficient of the wheels, μ_{dy} represents the lateral friction coefficient of the wheels also F_{nf} and F_{nr} are the normal forces on the front and rear wheels, respectively. Additionally, in Eq. (15), a velocity term is multiplied by sign functions, which, by taking derivatives from them, we will obtain the form of frictional force in the Gibbs-Appell equations. The normal forces on the wheel surfaces are obtained from the following relationships.

Front wheel normal force:

$$\begin{aligned} F_{nf} = {} & \frac{1}{l_x cos\,(\Psi) + l(cos\,(\alpha + \Psi) - cos\,(\beta + \Psi)\,)}(\frac{1}{2}M_G g(\frac{1}{2}l_x cos\,(\Psi) - lcos\,(\beta + \Psi)\,) \\ & + m_l g(l_x cos\,(\Psi) + \frac{1}{2}lcos\,(\alpha + \Psi) - \frac{3}{2}lcos\,(\beta + \Psi)\,)) \end{aligned} \tag{16}$$

Rear wheel normal force:

$$\begin{aligned} F_{nr} = {} & \frac{1}{l_x cos\,(\Psi) + l(cos\,(\alpha + \Psi) - cos\,(\beta + \Psi)\,)}(\frac{1}{2}M_G g(\frac{1}{2}l_x cos\,(\Psi) + lcos\,(\alpha + \Psi)\,) \\ & + m_l g(l_x cos\,(\Psi) + \frac{3}{2}lcos\,(\alpha + \Psi) - \frac{1}{2}lcos\,(\beta + \Psi)\,)) \end{aligned} \tag{17}$$

After formulating the Gibbs functions, potential function and friction function, these functions are incorporated into the final Gibbs equations to provide the dynamic equations for all pseudo-coordinates. The general form of the Gibbs equation, considering slip, is defined as

$$\frac{\partial S}{\partial \ddot{q}} + \frac{\partial D}{\partial \dot{q}} + \frac{\partial V}{\partial q} = \tau \tag{18}$$

where q represents the pseudo-coordinates of the system, and τ denotes the generalized torques (inputs). By incorporating each input into the equation above and taking derivatives, the governing dynamic equations for the system are derived. Notably, since 12 pseudo-coordinates have been obtained as independent coordinates, a set of 12 equations serves as the dynamic model for the robot. Furthermore, the formulation of the Gibbs–Appell method, Lagrange method, and their comparative analysis has been addressed

https://doi.org/10.1017/S0263574724001644 Published online by Cambridge University Press

in ref [33]. Next, by substituting pseudo accelerations in place of q for torques and forces acting on the system, the following quantities are extracted.

Torque of front leg motors:

$$\begin{aligned}\tau_\alpha = 2I_{ly}\ddot{\alpha} + \frac{1}{2}\Bigg(m_l\Bigg(-2\Bigg(\ddot{x} - \ddot{x}_{srf} - a\ddot{\theta}_{rf} + \frac{1}{2}\left(\ddot{\theta}l_y - l_x\ddot{\psi}sin\left(\psi\right) - l_x\dot{\psi}^2cos\left(\psi\right)\right)\\ -l\left(\ddot{\alpha}+\ddot{\psi}\right)sin\left(\alpha+\psi\right) - l\left(\dot{\alpha}+\dot{\psi}\right)^2cos\left(\alpha+\psi\right)\Bigg)lsin\left(\alpha+\psi\right)\\ +\Bigg(\ddot{z} - \ddot{z}_{srf} + \frac{1}{2}\Big(l_x\ddot{\psi}cos\left(\psi\right) - l_x\dot{\psi}^2sin\left(\psi\right) + l\left(\ddot{\alpha}+\ddot{\psi}\right)cos\left(\alpha+\psi\right) - l\left(\dot{\alpha}+\dot{\psi}\right)^2sin\left(\alpha+\psi\right)\Big)\\ l\,cos\left(\alpha+\psi\right) - 2\Bigg(\ddot{x} - \ddot{x}_{slf} - a\ddot{\theta}_{lf} + \frac{1}{2}\left(-\ddot{\theta}l_y - l_x\ddot{\psi}sin\left(\psi\right) - l_x\dot{\psi}^2cos\left(\psi\right)\right) - l\left(\ddot{\alpha}+\ddot{\psi}\right)\\ sin\left(\alpha+\psi\right) - l\left(\dot{\alpha}+\dot{\psi}\right)^2cos\left(\alpha+\psi\right)\Bigg)lsin\left(\alpha+\psi\right) + \Bigg(\ddot{z} - \ddot{z}_{slf} + \frac{1}{2}\Big(l_x\ddot{\psi}cos\left(\psi\right) - l_x\dot{\psi}^2\\ sin\left(\psi\right) + l\left(\ddot{\alpha}+\ddot{\psi}\right)cos\left(\alpha+\psi\right) - l\left(\dot{\alpha}+\dot{\psi}\right)^2sin\left(\alpha+\psi\right)\Big)l\,cos\left(\alpha+\psi\right)\Bigg)\Bigg)\end{aligned} \tag{19}$$

Torque of rear leg motors:

$$\begin{aligned}\tau_\beta = 2I_{ly}\ddot{\beta} + \frac{1}{2}\Bigg(m_l\Bigg(-2\Bigg(\ddot{x} - \ddot{x}_{srr} - a\ddot{\theta}_{rr} + \frac{1}{2}\left(\ddot{\theta}l_y + l_x\ddot{\psi}sin\left(\psi\right) + l_x\dot{\psi}^2cos\left(\psi\right)\right)\\ -l\left(\ddot{\beta}+\ddot{\psi}\right)sin\left(\beta+\psi\right) - l\left(\dot{\beta}+\dot{\psi}\right)^2cos\left(\beta+\psi\right)\Bigg)lsin\left(\beta+\psi\right) + (\ddot{z} - \ddot{z}_{srr}\\ +\frac{1}{2}\Big(-l_x\ddot{\psi}cos\left(\psi\right) + l_x\dot{\psi}^2sin\left(\psi\right) + l\left(\ddot{\beta}+\ddot{\psi}\right)cos\left(\beta+\psi\right) - l\left(\dot{\beta}+\dot{\psi}\right)^2sin\left(\beta+\psi\right)\Big)\\ l\,cos\left(\beta+\psi\right) - 2\Bigg(\ddot{x} - \ddot{x}_{slr} - a\ddot{\theta}_{lr} + \frac{1}{2}\left(-\ddot{\theta}l_y + l_x\ddot{\psi}sin\left(\psi\right) + l_x\dot{\psi}^2cos\left(\psi\right)\right) - l\left(\ddot{\beta}+\ddot{\psi}\right)\\ sin\left(\beta+\psi\right) - l\left(\dot{\beta}+\dot{\psi}\right)^2cos\left(\beta+\psi\right)\Bigg)lsin\left(\beta+\psi\right) + \Bigg(\ddot{z} - \ddot{z}_{slr} + \frac{1}{2}\Big(-l_x\ddot{\psi}cos\left(\psi\right)\\ +l_x\dot{\psi}^2sin\left(\psi\right) + l\left(\ddot{\beta}+\ddot{\psi}\right)cos\left(\beta+\psi\right) - l\left(\dot{\beta}+\dot{\psi}\right)^2sin\left(\beta+\psi\right)\Big)l\,cos\left(\beta+\psi\right)\Bigg)\Bigg)\end{aligned} \tag{20}$$

Torque of right front wheel motor:

$$\begin{aligned}\tau_{\theta rf} = I_o\ddot{\theta}_{rf} - m_l a(\ddot{x} - \ddot{x}_{srf} - a\ddot{\theta}_{rf} + \frac{1}{2}(\ddot{\theta}l_y - l_x\ddot{\psi}\,\sin\left(\psi\right) - l_x\dot{\psi}^2\cos\left(\psi\right)) - l\left(\ddot{\alpha}+\ddot{\psi}\right)\\ \sin\left(\alpha+\psi\right) - l\left(\dot{\alpha}+\dot{\psi}\right)^2\cos\left(\alpha+\psi\right))\end{aligned} \tag{21}$$

Torque of left front wheel motor:

$$\begin{aligned}\tau_{\theta lf} = I_o\ddot{\theta}_{lf} - m_l a(\ddot{x} - \ddot{x}_{slf} - a\ddot{\theta}_{lf} + \frac{1}{2}(-\ddot{\theta}l_y - l_x\ddot{\psi}\,\sin\left(\psi\right) - l_x\dot{\psi}^2\cos\left(\psi\right)) - l\left(\ddot{\alpha}+\ddot{\psi}\right)\\ \sin\left(\alpha+\psi\right) - l\left(\dot{\alpha}+\dot{\psi}\right)^2\cos\left(\alpha+\psi\right))\end{aligned} \tag{22}$$

Torque of right rear wheel motor:

$$\begin{aligned}\tau_{\theta rr} = I_o\ddot{\theta}_{rr} - m_l a(\ddot{x} - \ddot{x}_{srr} - a\ddot{\theta}_{rr} + \frac{1}{2}(\ddot{\theta}l_y + l_x\ddot{\psi}\,\sin\left(\psi\right) + l_x\dot{\psi}^2\cos\left(\psi\right)) - l\left(\ddot{\beta}+\ddot{\psi}\right)\\ \sin\left(\beta+\psi\right) - l\left(\dot{\beta}+\dot{\psi}\right)^2\cos\left(\beta+\psi\right))\end{aligned} \tag{23}$$

Torque of left rear wheel motor:

$$\begin{aligned}\tau_{\theta lr} = I_o\ddot{\theta}_{lr} - m_l a(\ddot{x} - \ddot{x}_{slr} - a\ddot{\theta}_{lr} + \frac{1}{2}(-\ddot{\theta}l_y + l_x\ddot{\psi}\,\sin\left(\psi\right) + l_x\dot{\psi}^2\cos\left(\psi\right)) - l\left(\ddot{\beta}+\ddot{\psi}\right)\\ \sin\left(\beta+\psi\right) - l\left(\dot{\beta}+\dot{\psi}\right)^2\cos\left(\beta+\psi\right))\end{aligned} \tag{24}$$

https://doi.org/10.1017/S0263574724001644 Published online by Cambridge University Press

Longitudinal friction force applied to the right front wheel:

$$F_{xsrf} = \frac{1}{2} m_l \left(-2\ddot{x} + 2\ddot{x}_{srf} + 2a\ddot{\theta}_{rf} - \ddot{\theta} l_y + l_x \ddot{\psi} sin\,(\psi) + l_x \dot{\psi}^2 cos\,(\psi) + 2l\left(\ddot{\alpha} + \ddot{\psi}\right)\right.$$
$$\left. sin\,(\alpha + \psi) + 2l\left(\dot{\alpha} + \dot{\psi}\right)^2 cos\,(\alpha + \psi)\right)$$
$$+ \frac{\mu_{dx}\left(\frac{1}{2} M_G g\left(\frac{1}{2} l_x\, cos\,(\psi) - l\, cos\,(\beta + \psi)\right) + m_l g\left(l_x\, cos\,(\psi) + \frac{1}{2}\left(l\, cos\,(\alpha + \psi) - 3l\, cos\,(\beta + \psi)\right)\right)\right)}{\left(l_x\, cos\,(\psi) + l\left(cos\,(\alpha + \psi) - cos\,(\beta + \psi)\right)\right)}. \tag{25}$$

Longitudinal friction force applied to the left front wheel:

$$F_{xslf} = \frac{1}{2} m_l \left(-2\ddot{x} + 2\ddot{x}_{slf} + 2a\ddot{\theta}_{lf} + \ddot{\theta} l_y + l_x \ddot{\psi} sin\,(\psi) + l_x \dot{\psi}^2 cos\,(\psi) + 2l\left(\ddot{\alpha} + \ddot{\psi}\right)\right.$$
$$\left. sin\,(\alpha + \psi) + 2l\left(\dot{\alpha} + \dot{\psi}\right)^2 cos\,(\alpha + \psi)\right)$$
$$+ \frac{\mu_{dx}\left(\frac{1}{2} M_G g\left(\frac{1}{2} l_x\, cos\,(\psi) - l\, cos\,(\beta + \psi)\right) + m_l g\left(l_x\, cos\,(\psi) + \frac{1}{2}\left(l\, cos\,(\alpha + \psi) - 3l\, cos\,(\beta + \psi)\right)\right)\right)}{\left(l_x\, cos\,(\psi) + l\left(cos\,(\alpha + \psi) - cos\,(\beta + \psi)\right)\right)}. \tag{26}$$

Longitudinal friction force applied to the right rear wheel:

$$F_{xsrr} = \frac{1}{2} m_l \left(-2\ddot{x} + 2\ddot{x}_{srr} + 2a\ddot{\theta}_{rr} + \ddot{\theta} l_y - l_x \ddot{\psi} sin\,(\psi) - l_x \dot{\psi}^2 cos\,(\psi) + 2l\left(\ddot{\beta} + \ddot{\psi}\right) sin\,(\beta + \psi)\right.$$
$$\left. + 2l\left(\dot{\beta} + \dot{\psi}\right)^2 cos\,(\beta + \psi)\right)$$
$$+ \frac{\mu_{dx}\left(\frac{1}{2} M_G g\left(\frac{1}{2} l_x\, cos\,(\psi) + l\, cos\,(\alpha + \psi)\right) + m_l g\left(l_x\, cos\,(\psi) + \frac{1}{2}\left(3l\, cos\,(\alpha + \psi) - l\, cos\,(\beta + \psi)\right)\right)\right)}{\left(l_x\, cos\,(\psi) + l\left(cos\,(\alpha + \psi) - cos\,(\beta + \psi)\right)\right)}. \tag{27}$$

Longitudinal friction force applied to the left rear wheel:

$$F_{xslr} = \frac{1}{2} m_l \left(-2\ddot{x} + 2\ddot{x}_{slr} + 2a\ddot{\theta}_{lr} + \ddot{\theta} l_y - l_x \ddot{\psi} sin\,(\psi) - l_x \dot{\psi}^2 cos\,(\psi) + 2l\left(\ddot{\beta} + \ddot{\psi}\right) sin\,(\beta + \psi)\right.$$
$$\left. + 2l\left(\dot{\beta} + \dot{\psi}\right)^2 cos\,(\beta + \psi)\right)$$
$$+ \frac{\mu_{dx}\left(\frac{1}{2} M_G g\left(\frac{1}{2} l_x\, cos\,(\psi) + l\, cos\,(\alpha + \psi)\right) + m_l g\left(l_x\, cos\,(\psi) + \frac{1}{2}\left(3l\, cos\,(\alpha + \psi) - l\, cos\,(\beta + \psi)\right)\right)\right)}{\left(l_x\, cos\,(\psi) + l\left(cos\,(\alpha + \psi) - cos\,(\beta + \psi)\right)\right)}. \tag{28}$$

Lateral friction force applied to the front wheels:

$$F_{ysf} = 2\mu_{dy}\left(\frac{1}{2} M_G g\left(\frac{1}{2} l_x\, cos\,(\psi) - l\, cos\,(\beta + \psi)\right) + m_l g\left(l_x\, cos\,(\psi) + \frac{1}{2}\left(l\, cos\,(\alpha + \psi)\right.\right.\right.$$
$$\left.\left.\left. - 3l\, cos\,(\beta + \psi)\right)\right)\right) / \left(l_x\, cos\,(\psi) + l\left(cos\,(\alpha + \psi) - cos\,(\beta + \psi)\right)\right). \tag{29}$$

Lateral friction force applied to the rear wheels:

$$F_{ysr} = 2\mu_{dy}\left(\frac{1}{2} M_G g\left(\frac{1}{2} l_x\, cos\,(\psi) + l\, cos\,(\alpha + \psi)\right) + m_l g\left(l_x\, cos\,(\psi) + \frac{1}{2}(3l\, cos\,(\alpha + \psi)\right.\right.$$
$$\left.\left. - l\, cos\,(\beta + \psi)\right)\right) / \left(l_x\, cos\,(\psi) + l\left(cos\,(\alpha + \psi) - cos\,(\beta + \psi)\right)\right). \tag{30}$$

https://doi.org/10.1017/S0263574724001644 Published online by Cambridge University Press

Table II. *Characteristics of motors in WLR joints.*

Parameters	Value	Unit
Accuracy of motors for reading angles	0.08	degree
XM540-W150-R no load speed	66	rpm
XL430-W250-T no load speed	61	rpm
XM540-W150-R torque stall	7.3	N.m.
XL430-W250-T torque stall	1.5	N.m.
XM540-W150-R gear ratio	152.3: 1	–
XL430-W250-T gear ratio	258.5: 1	–

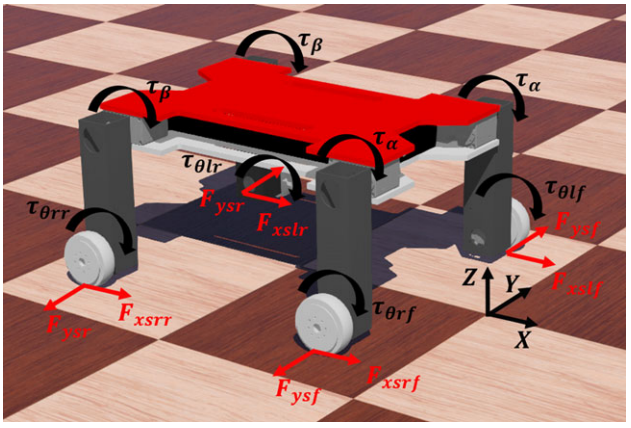

Figure 4. *Schematic of robot simulation in Webots, including operator torque and friction forces.*

4. Simulations and experimental results

As shown in Fig. 4, the behavior of the WLR has been simulated in the Webots software environment. Additionally, the kinematic and dynamic equations have been extracted using MATLAB and Maple software. By providing inputs to these equations, the behavior of the robot is simulated. Since slip is a random phenomenon and any behavior of it can have significant effects on the results, the simulation has been conducted considering a constant slip coefficient and compared with experimental results in order to validate them. Table II shows the characteristics of motors of WLR.

Fig. 5 illustrates the WLR used in experimental tests. The results of two experimental tests, one with the front wheels accelerating and inputs applied to these wheels, and the back wheels rolling freely, and the other with changing angles of both the front and back legs, have been compared with simulation results. In this experiment, it is assumed that the wheel slip coefficient and the surface are constant. We have demonstrated through the presentation of two distinct tests that alterations in the posture of the robot's body have proven to significantly impact the incidence of wheel slippage and subsequent modifications to the robot's movement patterns. In the robot test, placing equipment at the robot's center of mass improves movement and reduces slippage, as when the leg angles vary, the center of mass shifts toward the front and back of the robot, affecting the perpendicular force on the wheels and reducing the friction coefficient. Experimental test results were derived from the output data of the motors, motor encoders, and an inertial sensor attached to the body.

4.1. First test

As shown in Fig. 6, in the first test, the robot is in accelerating motion, with the back legs rotating from angles of 30 to 150 degrees and the front legs moving with a fixed angle of 30 degrees. The wheel

https://doi.org/10.1017/S0263574724001644 Published online by Cambridge University Press

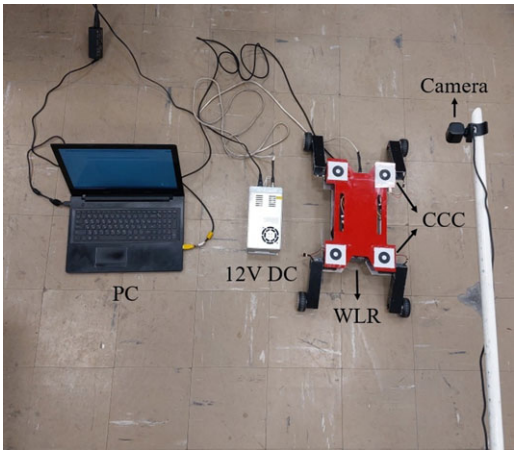

Figure 5. *Experimental setup.*

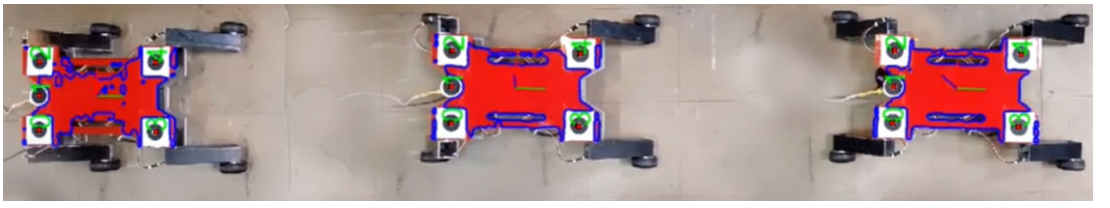

Figure 6. *Robot's motion in first test.*

speeds are set at an initial speed of zero, reaching a speed of 18.32 rev/min with an acceleration of 214.58 rev/min^2 for the front wheels. The legs have a constant speed of 3.44 rev/min. During this test, the wheels complete four rotations.

Fig. 7 shows the rotation of the robot's joint motors, with the back wheels (motors 5 and 8) in free mode and the front legs (motors 2 and 3) in fixed mode. The outcomes of the robot's behavior in the simulation environment closely align with the experimental data acquired from the encoder feedback of the motors. However, a slight variance in the acceleration of the motors has resulted in discrepancies in the initial movement results.

Fig. 8 shows the rotation speed of the joint motors of the robot. In the Webots simulator for test simulation and in experimental test, the back wheels are free-spinning. Due to the free movement of the back wheels (motors 5 and 8), their rotational speed accelerates with the movement of the body. Additionally, the speed of the back legs is constant in the Webots and experimental test. As the legs complete their rotation, the speed reaches zero (motors 1 and 4).

Fig. 9 shows the torque of the robot's joint motors. By considering the gravitational force, the mass of the robot, the inertia of the components, and the forces between the wheels and the ground surface, the torque applied to the motors can be determined. In the Webots software, the motors are designed to be close to the real model, which is why the output torque feedback of the motors is not as sharp and smooth. Also, taking into account the ground conditions and the forces acting on the wheels from the surface, a partial amount of torque is applied to the wheel motors, resulting in slightly different results from theoretical expectations. Additionally, a small amount of torque is applied to the back wheels due to changes in the angle of the legs and surface conditions. The results obtained from the motor torque show a consistent trend, decreasing as the robot body stabilizes.

https://doi.org/10.1017/S0263574724001644 Published online by Cambridge University Press

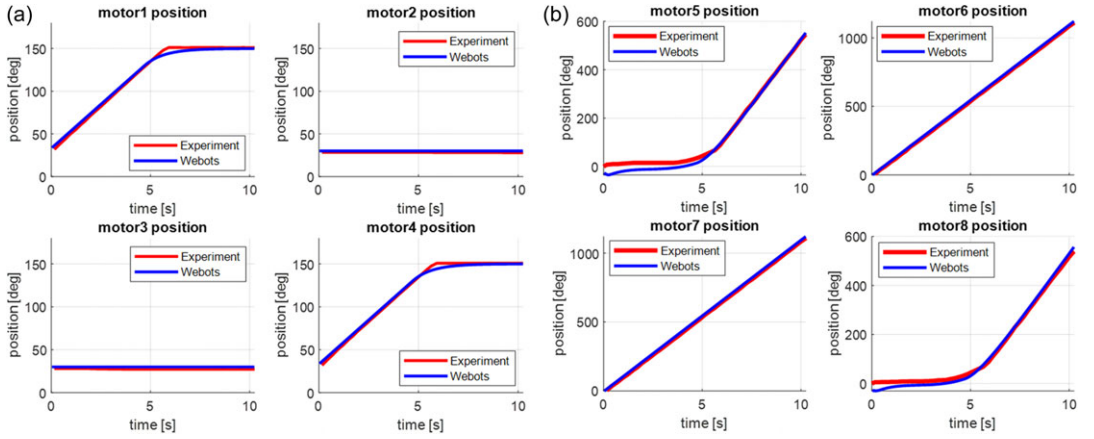

Figure 7. *Rotation of the robot's joint motors, (a) legs (b) wheels.*

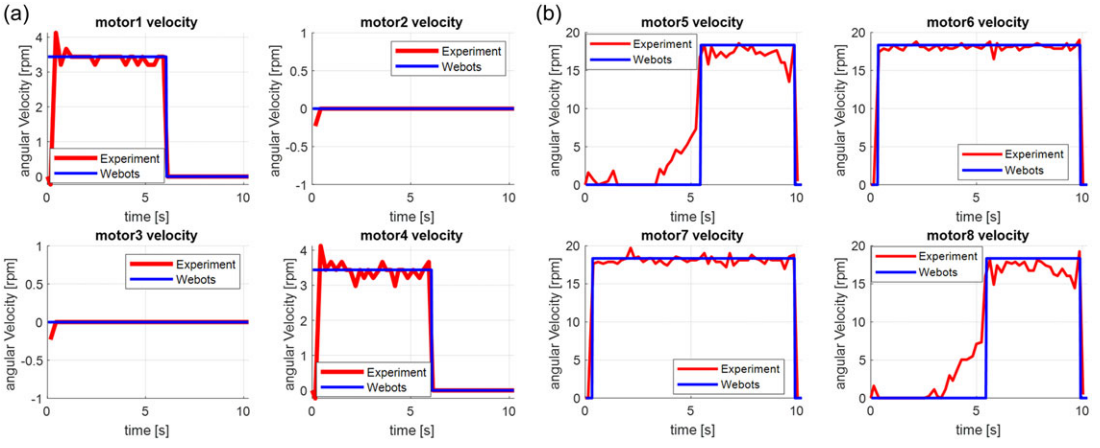

Figure 8. *Rotational speed of the robot's joint motors, (a) leg motors and (b) wheel motors.*

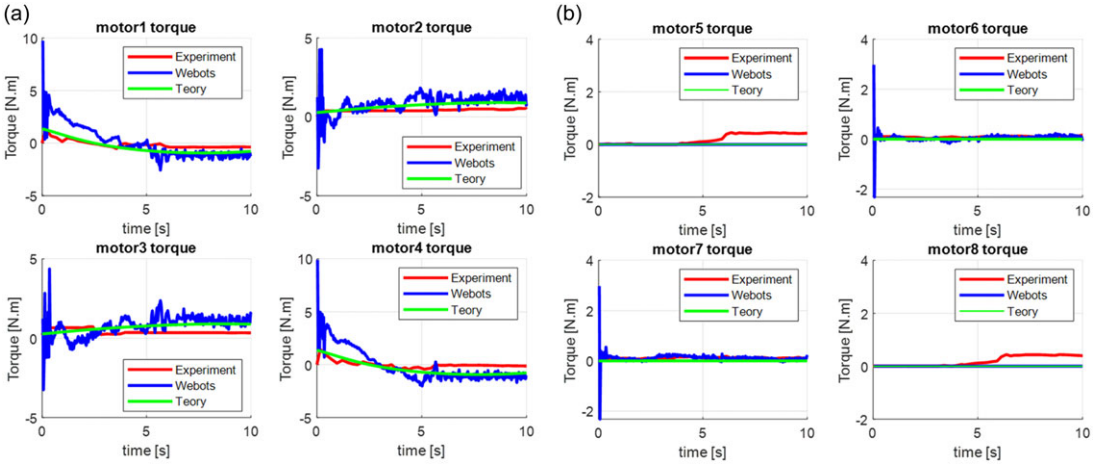

Figure 9. *Torque of the robot's joint motors, (a) leg motors and (b) wheel motors.*

https://doi.org/10.1017/S0263574724001644 Published online by Cambridge University Press

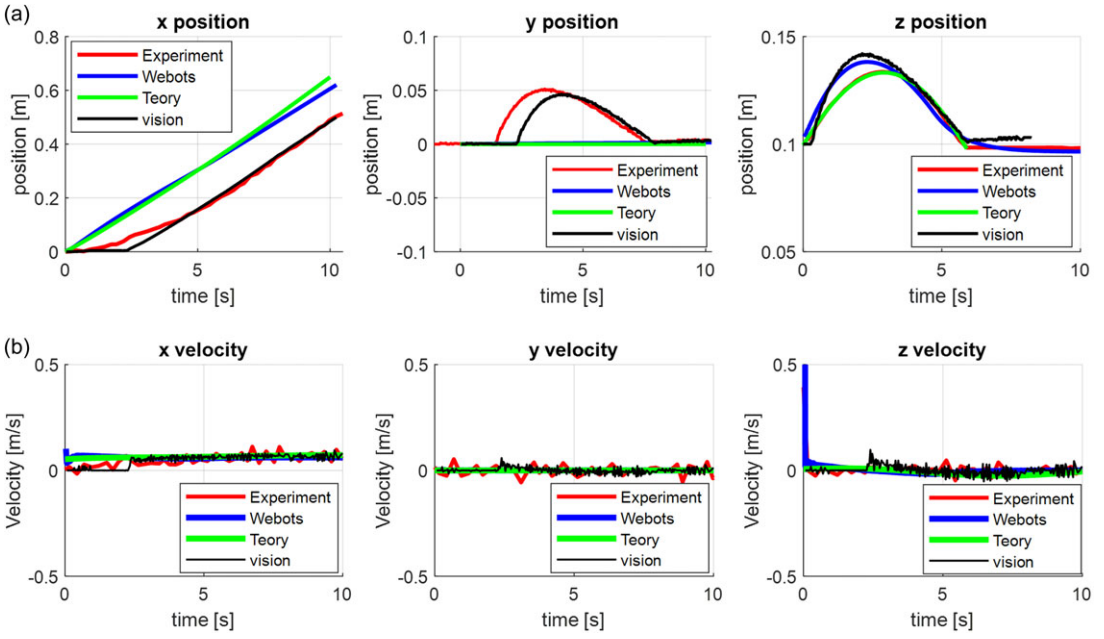

Figure 10. *Position and rotation angle of the robot, (a) linear position and (b) rotational position.*

In Fig. 10, the position and linear velocity of the robot's body in the direction of the specified coordinate axes are shown. The simulation outcomes in Webots, along with theoretical simulations conducted in MATLAB, exhibit a motion characterized by a consistent slip coefficient. However, in the experimental test, due to existing slippage, the behavior of the robot differs from theoretical results. Machine vision has effectively estimated the actual path of the robot's movement, and the experimental test data and machine vision are consistent with each other.

Fig. 11 shows the displacement of the robot on a two-dimensional plane. This image simulates observing the robot's center from above perpendicularly. The results indicate that the lateral displacement of the robot, especially at the beginning of the movement when the wheels slip, causes the robot's center to deviate from the straight path.

4.2. Second test

As shown in Fig. 12, in this test, the robot moves with an accelerating motion by changing the angle of its front legs from 30 to 150 degrees and its back legs from 150 to 30 degrees. This test was started with an initial speed of zero and reached a speed of 18.32 rev/min with an acceleration of 214.58 rev/min ^ 2 on the front wheels of the robot, while the front and back legs moved at a constant speed of 3.44 rev/min. The wheels in this test rotated four times.

Fig. 13 shows the rotation angle of the robot joint motors. The experimental test results acquired from the encoder feedback of the motors align well with the simulation outcomes and exhibit congruent movement behaviors. The rotation profile differs slightly between simulation in Webots and experimental test due to differences in applying acceleration to the motors of the robot.

Fig. 14 shows the rotation speed of the robot joint motors. In the Webots simulation for testing, a constant speed is given to the robot joints. However, in the experimental test, the joints start moving with acceleration as the motors are initially stationary to reach the ideal input as given. The software values in Webots are considered the set speed. The motor PID coefficients are very effective in changing the rotation profile and speed, affecting the motors' convergence speed with the input command. As the legs complete their rotation, the speed of motors drops to zero (motors 1 to 4). The back wheels are

https://doi.org/10.1017/S0263574724001644 Published online by Cambridge University Press

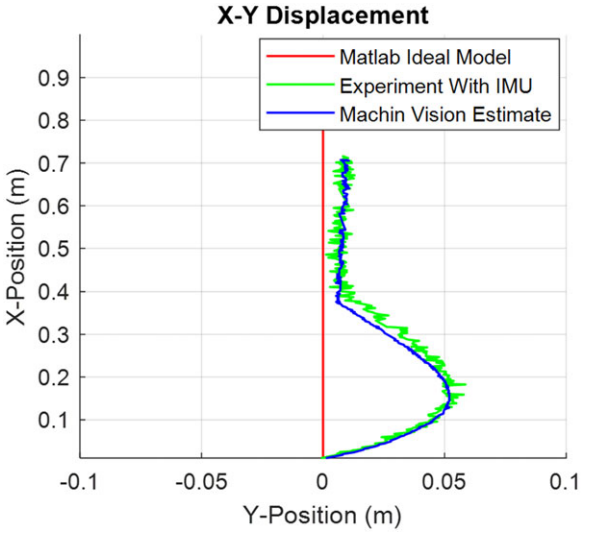

Figure 11. *The path traveled by the robot in first test.*

Figure 12. *Robot's motion in second test.*

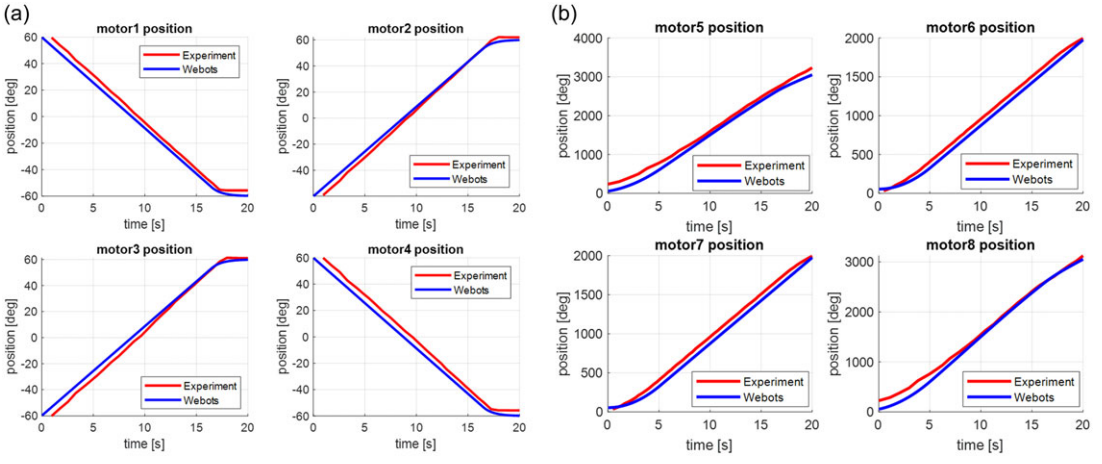

Figure 13. *Rotation angle of robot joint motors, (a) leg motors and (b) wheel motors.*

free-spinning. Because of this free movement, the rotational speed of the back wheels increases with the motion of the body. When the legs complete their movement, the speed of motors reaches zero (motors 5 and 8).

Fig. 15 shows the torque of the robot joints motors. In Webots software, the motors are designed closely to the real model, which is why the output torque feedback of the motors is not as sharp and smooth as the theoretical results. Due to the complexity of this test and differences in the motor's PID coefficients that determine the importance of input torque, and not seeing the applied torques from

https://doi.org/10.1017/S0263574724001644 Published online by Cambridge University Press

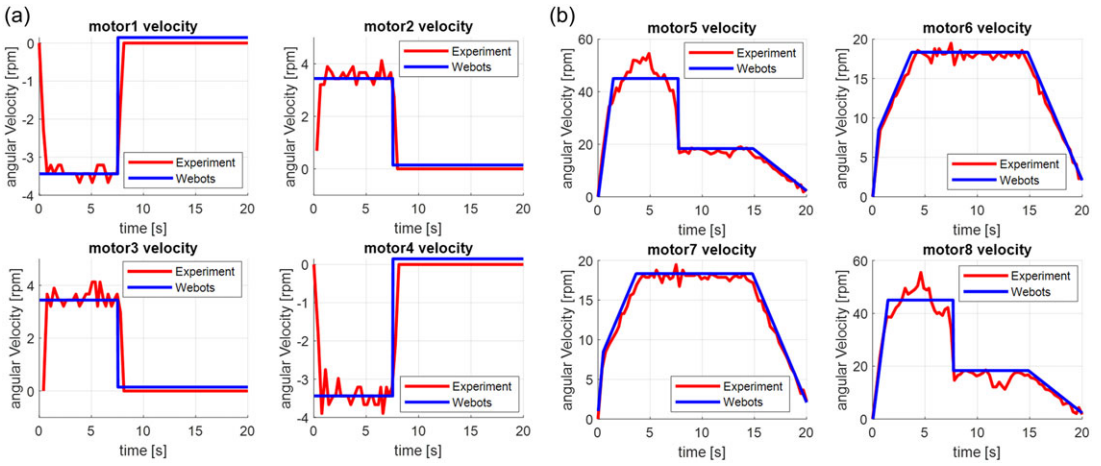

Figure 14. *Rotation speed of robot joint motors, (a) leg motors and (b) wheel motors.*

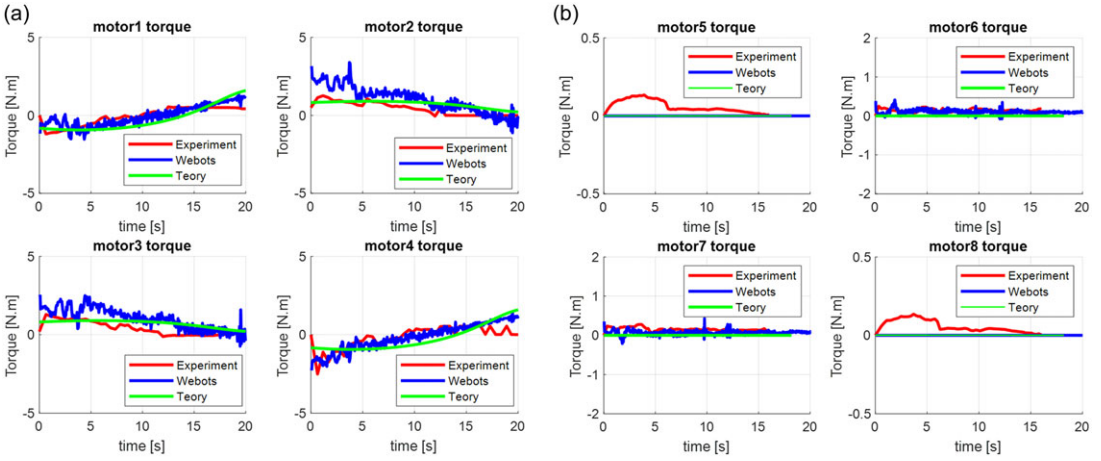

Figure 15. *Torque of robot joint motors, (a) leg motors and (b) wheel motors.*

other factors, the alignment of theoretical relationships with simulation has been slightly reduced to experimental testing.

In Fig. 16, the position and linear velocity of the robot body in the direction of specified coordinate axes are shown. The simulation outcomes within Webots, alongside the theoretical frameworks, both suggest a motion characterized by a consistent slip coefficient. However, disparities in the applied acceleration procedures between the two methods account for the variations observed. The machine vision results are close to the experimental test considering the existing slip, and the robot's behavior differs from theoretical results. Image processing has successfully estimated the robot's actual movement path, and the experimental test data and image processing are consistent with each other. Furthermore, the inertial sensor and image processing worked well in determining the robot's position in real conditions and were able to estimate the deviation of the robot from the main path under slip conditions and measure changes in the body's height with good accuracy consistent with simulation.

Fig. 17 shows the displacement of the robot on a two-dimensional plane. This image depicts the overall movement of the robot on the plane and its trajectory. The ideal movement state of the robot is straight motion without lateral displacement; however, the results indicate that the lateral displacement of the robot at the beginning of the movement, when the wheels slip, causes the robot to deviate from the main path. At the end of the path, due to the body's deviation from the path, significant lateral displacement occurs.

https://doi.org/10.1017/S0263574724001644 Published online by Cambridge University Press

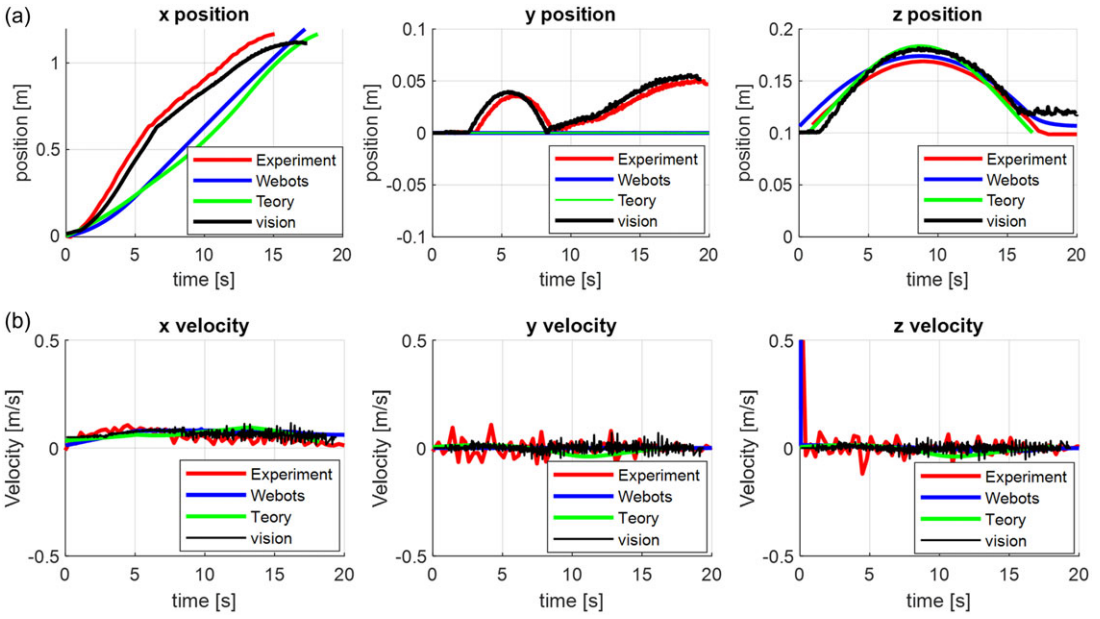

Figure 16. *Position and rotation angle of the robot, (a) linear position and (b) rotational position.*

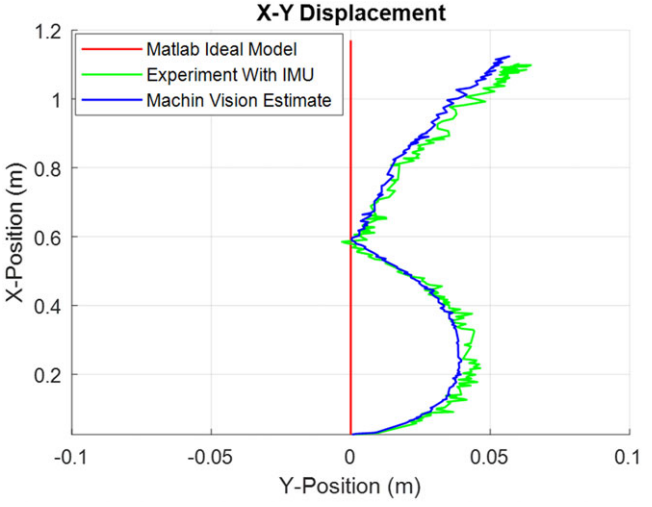

Figure 17. *The path traveled by the robot in second test.*

5. Conclusion

This research focuses on the development of a mathematical formulation related to the kinematic and dynamic modeling of a WLR with the assumption of slipping to improve the accuracy of these equations. In the first step, kinematic equations were derived using vector methods, and then dynamic equations were extracted using the Gibbs–Appell formulation. By utilizing pseudo-acceleration equations and Gibbs functions, the forces and torques acting on the robot's actuators were obtained. In comparison to recent works, this method reduces the number of equations and computational complexity. In previous studies, classic or intelligent estimators have often been used to estimate slippage, with less emphasis on measuring actual slip in experimental tests. However, in this research, a slip estimation method based on machine vision were used to determine the slippage of the wheels and body center velocity of the

https://doi.org/10.1017/S0263574724001644 Published online by Cambridge University Press

robot's motion at each moment in the motion space. The longitudinal and lateral slip of each wheel and the body slip at each moment were extracted for use in the developed equations. Furthermore, to validate the developed equations, the WLR was modeled in the Webots software environment, and the results obtained from this software were compared with the results of simulations in MATLAB software and experimental results. The experimental results were compared with theoretical and simulation results under two different motion scenarios: once with the front wheels accelerating and inputs applied to these wheels while the rear wheels freely rotating and again with changes in the rear leg angles while keeping the front legs fixed and once more with changes in both front and rear leg angles. The results of this comparison clearly indicate an acceptable similarity between the experimental data and the simulation results. The findings indicated that assuming a consistent slip coefficient in the robot's motion modeling led to an 11.5% error in accelerated straight movement when the rear legs rotated, and a 5% error in accelerated straight movement when both the rear and front legs rotated. To reduce modeling errors, the effects of longitudinal and lateral slip of each wheel of the robot should be considered as input terms in the modeling system. This will make the robot's modeling closer to its actual movement. Additionally, slipping effects can be minimized by changing the type of tires to more adhesive ones, increasing the robot's weight, or altering the robot's movement surface to one with a higher coefficient of friction. To measure slip, GPS sensors, motion detection sensors, and IMU sensors can be utilized in addition to machine learning methods. By fusing their data with machine learning data, the accuracy of slip measurement and error rate can be improved. Additionally, the lateral slippage for each of the tests was, respectively, 1.1 and 5.2 cms, indicating that the robot deviated to the sides and that lateral slippage should be considered in the modeling to achieve more accurate results. In general, this work can be considered a positive step toward improving the accuracy of recent works on theoretical aspects, as well as enhancing the reliability of WLRs in practical applications.

Author contributions. Korayem and Nikseresht conceived and designed the study. Nikseresht conducted data gathering. Nikseresht and Asadi performed simulation analyses. Nikseresht and Asadi wrote the article.

Financial support. This research received no specific grant from any funding agency, commercial, or not-for-profit sectors.

Competing interests. The authors declare no conflicts of interest exist.

Ethical approval. Not applicable.

References

[1] G. Thomas and V. V. Vantsevich, "Wheel-terrain-obstacle interaction in vehicle mobility analysis," *Veh. Syst. Dyn.* **48**(S1), 139–156 (2010).
[2] S. Singh and K. M. Krishna, "Gait sequence generation of a hybrid wheeled-legged robot for negotiating discontinuous terrain," **In:** *IEEE International Conference on Control Applications (CCA) 2013 Aug 28*., Hyderabad, India IEEE (2013) 766–771.
[3] J. Niu, H. Wang, H. Shi, N. Pop, D. Li, S. Li and S. Wu, "Study on structural modeling and kinematics analysis of a novel wheel-legged rescue robot," *Int. J. Adv. Robot. Syst.* **15**(1), 1729881417752758 (2018).
[4] W. Reid, B. Emanuel, B. Chamberlain-Simon, S. Karumanchi and G. Meirion-Griffith, "Mobility mode evaluation of a wheel-on-limb rover on glacial ice analogous to europa terrain," **In:** *IEEE Aerospace Conference 2020*, Big Sky, MT, USA IEEE (2020) 1–9.
[5] M. Geilinger, S. Winberg and S. Coros, "A computational framework for designing skilled legged-wheeled robots," *IEEE Robot. Autom. Lett.* **5**(2), 3674–3681 (2020).
[6] J. A. Smith, I. Sharf and M. Trentini, "PAW: a hybrid wheeled-leg robot," **In:** *Proceedings. 2006 IEEE International Conference on Robotics and Automation, 2006. ICRA 2006, Orlando, FL, USA* IEEE (2006) 4043–4048.
[7] A. Toorani, M. H. Korayem and A. H. Davaie Markazi, "Kinematic and dynamic analysis of a nonholonomic wheel-legged robot using Gibbs-Appell formulation," *J. Braz. Soc. Mech. Sci.* **46**(3), 159 (2024).
[8] H. Mirzaeinejad and A. M. Shafei, "Modeling and trajectory tracking control of a two-wheeled mobile robot: Gibbs-Appell and prediction-based approaches," *Robotica* **36**(10), 1551–1570 (2018).
[9] V. Mata, S. Provenzano, J. L. Cuadrado and F. Valero, "Inverse dynamic problem in robots using Gibbs-Appell equations," *Robotica* **20**(1), 59–67 (2002).
[10] M. H. Korayem, M. V. Ardalani and A. Toorani, "Stability analysis and implementation of a wheel-leg robot using the Force-Angle method," *Arab. J. Sci. Eng.* **48**(9), 11379–11389 (2023).

https://doi.org/10.1017/S0263574724001644 Published online by Cambridge University Press

[11] P. Arunkumar, A. P. Sudheer and M. L. Joy, "Kinematic modelling and analysis of single leg in hybrid wheel-legged mobile robot," **In:** *IOP Conference Series: Materials Science and Engineering 2021*, IOP Publishing, **1132**(1), 012035 (2021).
[12] A. Alamdari and V. Krovi, "Active reconfiguration for performance enhancement in articulated wheeled vehicles," **In:** *Proceedings of the ASME 2014 Dynamic Systems and Control Conference. Volume 2: Dynamic Modeling and Diagnostics in Biomedical Systems; Dynamics and Control of Wind Energy Systems; Vehicle Energy Management Optimization; Energy Storage, Optimization; Transportation and Grid Applications; Estimation and Identification Methods, Tracking, Detection, Alternative Propulsion Systems; Ground and Space Vehicle Dynamics; Intelligent Transportation Systems and Control; Energy Harvesting; Modeling and Control for Thermo-Fluid Applications, IC Engines, Manufacturing*, San Antonio, Texas, USA, October 22–24 (2014) V002T27A004.
[13] W. Du, M. Fnadi and F. Benamar, "Rolling based locomotion on rough terrain for a wheeled quadruped using centroidal dynamics," *Mech. Mach. Theory.* **153**, 103984 (2020).
[14] W. Reid, F. J. Pérez-Grau, A. H. Göktoğan and S. Sukkarieh, "Actively articulated suspension for a wheel-on-leg rover operating on a martian analog surface," **In:** *IEEE International Conference on Robotics and Automation (ICRA) 2016 May 16*, Stockholm, Sweden IEEE (2016) 5596–5602.
[15] C. Grand, F. B. Amar and P. Bidaud. "Kinematic Analysis and Stability Optimization of a Reconfigurable Legged-Wheeled Mini-Rover.," **In:** *SPIE Proceedings*, Orlando, FL, United States, SPIE Digitial Library **4715**, (2002) pp. 295–302.
[16] B. Beckman, J. Pieper, D. Mackay, M. Trentini and D. Erickson, "Two dimensional dynamic stability for reconfigurable robots designed to traverse rough terrain," **In:** *IEEE/RSJ International Conference on Intelligent Robots and Systems 2008 Sep 22*, Nice, France IEEE (2008) 2447–2452.
[17] V. S. Medeiros, E. Jelavic, M. Bjelonic, R. Siegwart, M. A. Meggiolaro and M. Hutter, "Trajectory optimization for wheeled-legged quadrupedal robots driving in challenging terrain," **In:** *IEEE Robotics and Automation Letters* **5**(3), 4172–4179 (2020).
[18] G. Ishigami, K. Nagatani and K. Yoshida, "Path planning for planetary exploration rovers and its evaluation based on wheel slip dynamics," **In:** *Proceedings 2007 IEEE International Conference on Robotics and Automation 2007 Apr 10*, Roma, Italy IEEE (2007) 2361–2366.
[19] M. Bjelonic, P. K. Sankar, C. D. Bellicoso, H. Vallery and M. Hutter, "Rolling in the deep-hybrid locomotion for wheeled-legged robots using online trajectory optimization," *IEEE Robotics and Automation Letters* **5**(2), 3626–3633 (2020).
[20] Y. Watanabe and K. Nonaka, "Slip measurement and vehicle control for leg/wheel mobile robots using caster type odometers," **In:** *IEEE International Conference on Control Applications (CCA) 2011 Sep 28*, Denver, CO, USA IEEE (2011) 681–686.
[21] D. Lhomme-Desages, C. Grand and J. C. Guinot, "Trajectory control of a four-wheel skid-steering vehicle over soft terrain using a physical interaction model," **In:** *Proceedings 2007 IEEE International Conference on Robotics and Automation*, Rome, Italy, IEEE (2007) 1164–1169.
[22] E. I. Al Khatib, M. A. Jaradat, M. Abdel-Hafez and M. Roigari, "Multiple sensor fusion for mobile robot localization and navigation using the Extended Kalman Filter," **In:** *10th international symposium on mechatronics and its applications (ISMA) 2015 Dec 8*, Sharjah, United Arab Emirates, IEEE (2015) 1–5.
[23] A. H. Asadi, N. Nikseresht and A. H. Korayem, "Adaptive MIMO PID Control of a Wheel-Leg Manipulator by Considering the Slippage Based on Deep Reinforcement Learning," **In:** *11th RSI International Conference on Robotics and Mechatronics (ICRoM) 2023 Dec 19*, Tehran, Iran IEEE (2023) 437–442.
[24] Z. Li, Y. Wang and Z. Liu, "Unscented Kalman filter-trained neural networks for slip model prediction," *PloS one* **11**(7), e0158492 (2016).
[25] A. Botta, P. Cavallone, L. Tagliavini, L. Carbonari, C. Visconte and G. Quaglia, "An estimator for the kinematic behaviour of a mobile robot subject to large lateral slip," *Appl. Sci.* **11**(4), 1594 (2021).
[26] D. Lhomme-Desages, C. Grand, F. B. Amar and J. C. Guinot, "Doppler-based ground speed sensor fusion and slip control for a wheeled rover," *IEEE/ASME Trans. Mechatron.* **14**(4), 484–492 (2009).
[27] J. Guo, W. Li, L. Ding, T. Guo, H. Gao, B. Huang and Z. Deng, "High-slip wheel-terrain contact modelling for grouser-wheeled planetary rovers traversing on sandy terrains," *Mech. Mach. Theory.* **153**, 104032 (2020).
[28] G. Reina, "Methods for Wheel Slip and Sinkage Estimation in Mobile Robots," **In:** *Robot Localization and Map Building*, IntechOpen, (2010).
[29] G. Reina, L. Ojeda, A. Milella and J. Borenstein, "Wheel slippage and sinkage detection for planetary rovers," *IEEE/ASME Trans. Mechatron.* **11**(2), 185–195 (2006).
[30] N. Nikseresht, M. H. Korayem and A. Toorani, "Modeling and simulation of a wheel-leg robot," **In:** *10th RSI International Conference on Robotics and Mechatronics (ICRoM) 2022 Nov 22*, Tehran, Iran IEEE (2022) 178–183.
[31] E. Pennestrì, V. Rossi, P. Salvini and P. P. Valentini, "Review and comparison of dry friction force models," *Nonlinear Dyn.* **83**(4), 1785–1801 (2016).
[32] F. Marques, P. Flores, J. C. Pimenta Claro and H. M. Lankarani, "A survey and comparison of several friction force models for dynamic analysis of multibody mechanical systems," *Nonlinear Dyn.* **86**(3), 1407–1443 (2016).
[33] E. Desloge, "The Gibbs-Appell equations of motion," *Am. J. Phys.* **56**(9), 841 (1988).

Cite this article: M. H. Korayem, N. Nikseresht and A. H. Asadi, "Vision-based dynamic modeling of wheeled-legged robot considering slippage using Gibbs–Appell formulation", Robotica. https://doi.org/10.1017/S0263574724001644